

# The $L_X-T_{\text{vir}}$ relation in galaxy clusters: Effects of radiative cooling and AGN heating

Rupal Mittal<sup>1,2</sup>, Amalia Hicks<sup>3</sup>, Thomas H. Reiprich<sup>2</sup>, and Vera Jaritz<sup>2</sup>

<sup>1</sup> Center of Imaging Science, Rochester Institute of Technology, 54 Lomb Memorial Drive, Rochester, NY, USA 14623

<sup>2</sup> Argelander-Institut für Astronomie, Auf dem Hügel 71, 53121 Bonn, Germany

<sup>3</sup> Michigan State University, Physics and Astronomy Dept., East Lansing, MI 48824-2320, USA

Received/Accepted

**Abstract.** We present a detailed investigation of the X-ray luminosity ( $L_X$ )-gas temperature ( $T_{\text{vir}}$ ) relation of the complete X-ray flux-limited sample of the 64 brightest galaxy clusters in the sky (*HIFLUGCS*). We study the influence of two astrophysical processes, active galactic nuclei (AGN) heating and intracluster medium (ICM) cooling, on the  $L_X-T_{\text{vir}}$  relation, simultaneously for the first time. We employ homogeneously determined gas temperatures and central cooling times, measured with *Chandra*, and information about a central radio source from Mittal and collaborators. We determine best-fit relations for different subsamples using the cool-core strength and the presence of central radio activity as selection criteria. We find the strong cool-core clusters (SCCs) with short cooling times ( $< 1$  Gyr) to display the steepest relation ( $L_X \propto T_{\text{vir}}^{3.33 \pm 0.15}$ ) and the non-cool-core clusters (NCCs) with long cooling times ( $> 7.7$  Gyr) to display the shallowest ( $L_X \propto T_{\text{vir}}^{2.42 \pm 0.21}$ ). This has the simple implication that on the high-mass scale ( $T_{\text{vir}} > 2.5$  keV) the steepening of the  $L_X-T_{\text{vir}}$  relation is mainly due to the cooling of the intracluster medium gas. We propose that ICM cooling and AGN heating are both important in shaping the  $L_X-T_{\text{vir}}$  relation but on different length-scales. While our study indicates that ICM cooling dominates on cluster scales ( $T_{\text{vir}} > 2.5$  keV), we speculate that AGN heating dominates the scaling relation in poor clusters and groups ( $T_{\text{vir}} < 2.5$  keV).

The intrinsic scatter about the  $L_X-T_{\text{vir}}$  relation in X-ray luminosity for the whole sample is 45.4% and varies from a minimum of 34.8% for weak cool-core clusters to a maximum of 59.4% for clusters with no central radio source. The scatter does not decrease if SCC clusters are excluded from the full sample. We find that the contribution of core luminosities within the cooling radius  $r_{\text{cool}}$ , where the cooling time is 7.7 Gyr and gas cooling may be important, to the total X-ray luminosities amounts to 44% and 15% for the SCC and WCC clusters, respectively. We find that after excising the cooling region, the scatter in the  $L_X-T_{\text{vir}}$  relation drops from 45.4% to 39.1%, implying that the cooling region contributes  $\sim 27\%$  to the overall scatter. The remaining scatter is largely due to the NCCs.

Lastly, the statistical completeness of the sample allows us to quantify and correct for selection effects individually for the subsamples. We find the true SCC fraction to be 25% lower than the observed one and the true normalizations of the  $L_X-T_{\text{vir}}$  relations to be lower by 12%, 7%, and 17% for SCC, WCC, and NCC clusters, respectively.

## 1. Introduction

Scaling relations in galaxy clusters and groups are of great interest for the determination of cosmological key parameters (e.g. Borgani & Guzzo 2001; Rosati et al. 2002; Reiprich & Böhringer 2002; Stanek et al. 2006; Reiprich 2006; Mantz et al. 2008; Vikhlinin et al. 2009; Leauthaud et al. 2010). Of prime importance is to keep track of the systematics that enter the slope and normalization determination due to different physical mechanisms. These physical processes may, for example, be related to AGN activity, sloshing or bulk motions of gas, or cooling of the intracluster medium (ICM).

In the context of cooling flows and AGN heating, there is still a considerable amount of debate about the X-ray luminosity ( $L_X$ )-temperature ( $T_{\text{vir}}$ ) relation (e.g. Markevitch 1998; Voit & Bryan 2001; Fabian et al. 1994; Bower et al. 2008; Magliocchetti & Brüggen 2007; McCarthy et al. 2004). The

$L_X-T_{\text{vir}}$  relation currently faces two main challenges. Firstly, the slope as determined from observations is much higher ( $L_X \propto T_{\text{vir}}^{2.5-3.0}$ , Allen & Fabian 1998; Arnaud & Evrard 1999) than that predicted based on the self-similarity of halos ( $L_X \propto T_{\text{vir}}^{2.0}$ , Kaiser 1986; Eke et al. 1998). Secondly, the intrinsic dispersion (excluding statistical errors) in the relation is large, which diminishes its utility in constraining cosmological parameters. As per the results of Pratt et al. (2009), the raw scatter about the  $L_X-T_{\text{vir}}$  relation is about 70% in  $L_X$ , which decreases significantly on excising the cluster central regions (see Section 4). Both these findings illustrate our lack of understanding of the physics that governs the formation and evolution of the largest virialized structures in the Universe. As a first step towards using galaxy clusters as cosmological tools, we need to address variations in their physical and structural properties caused by baryon processes, such as radiative

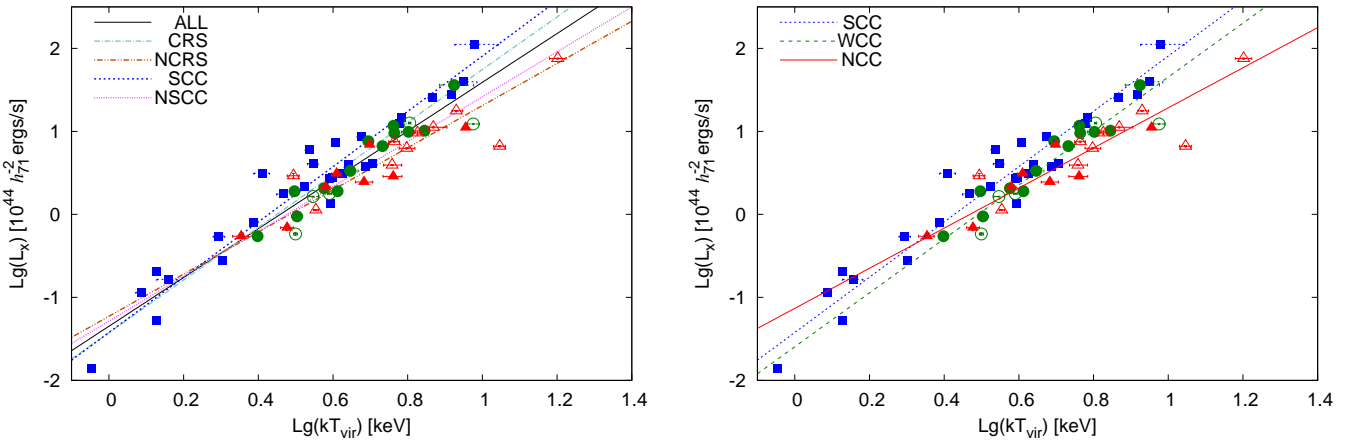


**Fig. 1.**  $L_X-T_{\text{vir}}$  relation for the HIFLUGCS sample of clusters. The filled symbols represent clusters with a central radio source and the open symbols represent those without. The squares (blue), circles (green), and triangles (red) represent strong cool-core clusters ( $t_{\text{cool}} < 1$  Gyr), weak cool-core clusters ( $1 \text{ Gyr} < t_{\text{cool}} < 7.7$  Gyr), and non-cool-core clusters ( $t_{\text{cool}} > 7.7$  Gyr), respectively.

cooling, heating due to AGN or conduction, and eradicate their effects on the scaling relations.

Several works, based on both observations and simulations, have indicated that the  $L_X-T_{\text{vir}}$  relation in low-mass halos with a central radio source differs systematically from that in systems without a central radio source (Sijacki & Springel 2006; Croston et al. 2005; Puchwein et al. 2008). Studies also show that clusters with strong cooling, as indicated by either the short cooling times of the intracluster gas or high classical gas mass deposition rates, lie on a different  $L_X-T_{\text{vir}}$  plane (e.g., Allen & Fabian 1998; O’Hara et al. 2006). In this work, we extend these studies to understand the behaviour of the  $L_X-T_{\text{vir}}$  relation in the presence of both AGN heating and ICM cooling. The sample we use to do this is the complete flux-limited HIFLUGCS sample (Reiprich & Böhringer 2002), constituting the 64 X-ray brightest galaxy clusters with high-quality *Chandra* data (Hudson et al. 2010) and radio data with good spectral coverage (Mittal et al. 2009) for all the clusters. Thus, a rich database of X-ray and radio data allows us to study the influence of both the mechanisms in parallel.

This article is organized as follows. In section 2, we describe the data used for the work and the data analysis. In section 3, we outline the subsamples created based on the radio and cooling properties and compare the individual  $L_X-T_{\text{vir}}$  fits. In section 4, we scrutinize the cooling activity as the main cause of the scatter about the observed  $L_X-T_{\text{vir}}$  relation. In section 5, we investigate systematics, such as the selection effects that might bias the observed fractions of the different type of cool-core clusters and whether the new Chandra calibration has any impact on the slope of the fitted  $L_X-T_{\text{vir}}$  relations. Finally, in sections 6 and 7, we discuss our results and present our conclusions. We assume throughout this paper a  $\Lambda$ CDM concordance Universe, with  $H_0 = 71 h_{71}$  km/s/Mpc,  $\Omega_m = 0.27$ , and  $\Omega_\Lambda = 0.73$ .

## 2. Data and analysis

In this section, we present a brief introduction of the datasets and quantities used in this work. The data reduction and analysis can be found in detail in Hudson et al. (2010) [hereafter H10] for the X-ray data and Mittal et al. (2009) [hereafter M09] for the radio data.

The study in H10 used  $> 4.5$  Ms of high-resolution *Chandra* data and provided a detailed census of the inner regions of clusters offering an insight into the physics governing cluster cores. It summarized 16 different cool-core diagnostics and found that the central cooling time,  $t_{\text{cool}}$ , was the best indicator. This choice resulted in 44% strong cool-cores (SCC) with  $t_{\text{cool}} < 1 h_{71}^{1/2}$  Gyr, 28% weak cool-cores (WCC) with  $1 h_{71}^{1/2}$  Gyr  $< t_{\text{cool}} < 7.7 h_{71}^{1/2}$  Gyr and another 28% non-cool-cores (NCC) with  $t_{\text{cool}} > 7.7 h_{71}^{1/2}$  Gyr. Following this result, we use  $t_{\text{cool}}$  as the measure of the cooling strength of a cluster, such that those with shorter  $t_{\text{cool}}$  have higher cooling strengths.

M09 utilized more than 140 different radio flux-density measurements in their study and obtained the total radio luminosities for correlation with cooling properties. They also determined the fraction of central radio sources (CRSs) in the HIFLUGCS sample and found that 48 out of 64 clusters (75%) contain cluster-centre radio sources that are either cospatial with or within  $50 h_{71}^{-1}$  kpc of the X-ray peak emission. In addition, M09 found that the probability of finding a cluster-centre radio source increases with cooling strength, from 45% to 67%<sup>1</sup> to 100% for NCC, WCC and SCC clusters, respec-

<sup>1</sup> In the meantime, one more WCC cluster (A1650) has been found, owing to higher sensitivity of the more recent radio observations, to harbour a central radio source (Govoni et al. 2009), increasing the total number of cluster-centre radio sources from 48 to 49 and the fraction of CRSs in the WCC category from 67% to 72%.

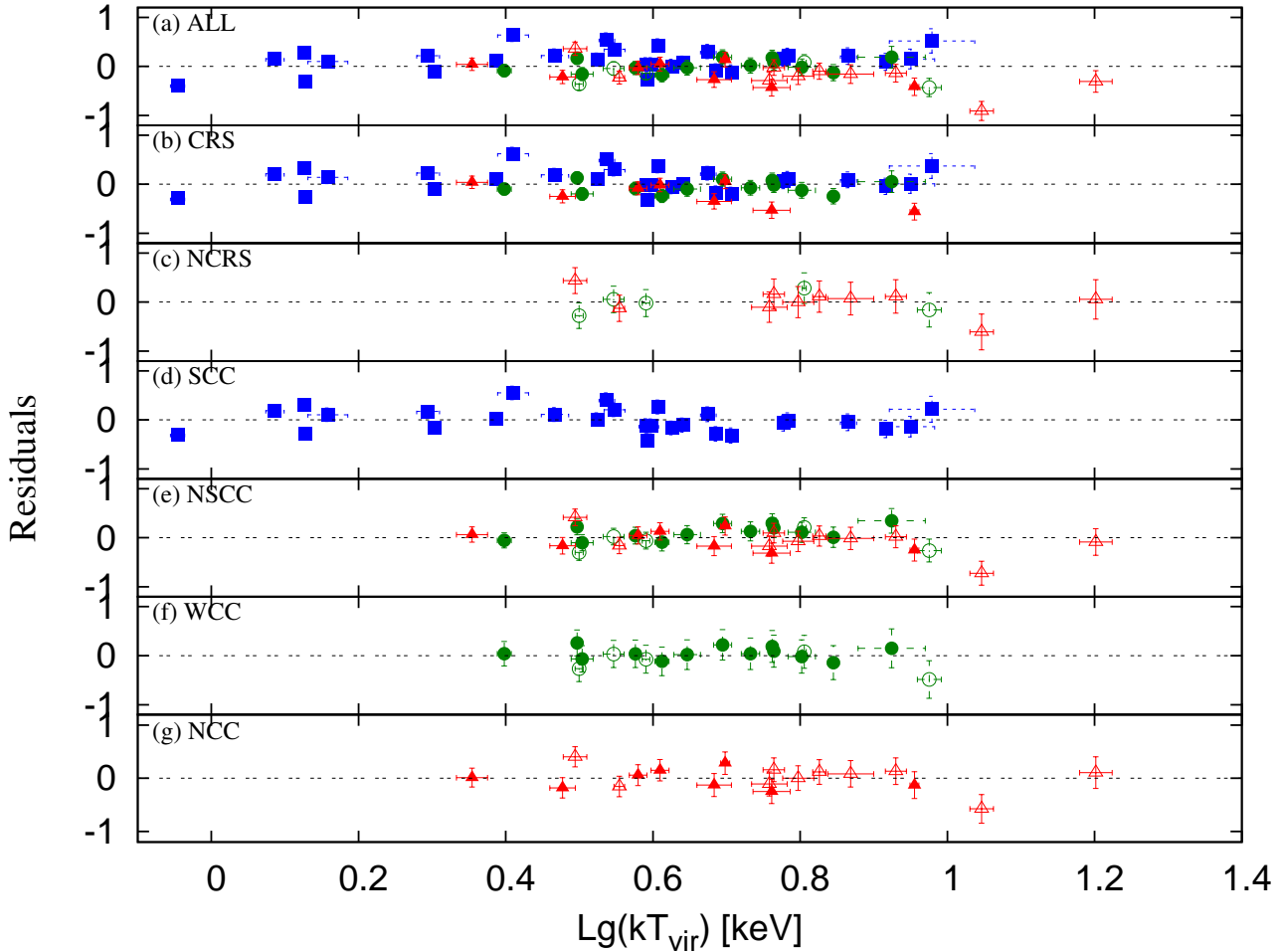


**Fig. 2.** The lg-space residuals in  $L_X$  for each category with respect to their individual best fits. The symbol representation is the same as in Fig. 1. The errorbars for each subgroup are obtained from summing the uncertainties in the measured and the fitted luminosities in quadrature. The fitted luminosities for a subgroup are obtained through the best-fit  $L_X-T_{\text{vir}}$  relation of that subgroup

tively. This provides evidence of a connection between the supermassive black hole activity and the cooling of the ICM.

The virial temperatures,  $T_{\text{vir}}$ , were taken from H10. The authors determined  $T_{\text{vir}}$  by removing the central region of the observed *Chandra* temperature profile. This was done in order to prevent the cool-core region from corrupting the global cluster temperature estimates. To determine the size of the central region to be excluded, we fitted the temperature profiles to a broken power-law. The radius of the central region in the power-law was free and the index of the outer component was fixed to be zero. Owing to the limited field-of-view of *Chandra*, the outer radius for the  $T_{\text{vir}}$  determination varies. This may introduce a small amount of scatter, although, tests on two of the highest-redshift clusters in the sample, A2204 and A2163, indicate that our conclusions are not affected by this.

The bolometric X-ray cluster luminosities over the range (0.01 to 40) keV,  $L_X$ , as measured with *ROSAT* using mostly

ASCA temperatures, were taken from Reiprich & Böhringer (2002). *ROSAT* data were preferred over those of *Chandra* for the total cluster luminosities because *ROSAT* has a larger field of view and a lower instrumental background than *Chandra*. The errors in the bolometric luminosities are reflective of the errors in the count rate. Temperature uncertainties, which are on the order of 10% (Reiprich & Böhringer 2002), form an additional source of statistical scatter. On the basis of on simulations using PIMMS (portable, interactive multi-mission simulator) and theoretical grounds ( $L_X \sim T_{\text{vir}}^{0.5}$ ), a 10% error in temperature implies a  $\sim 5\%$  error in  $L_X$ . Although we do not take this additional uncertainty into account, one may conservatively add a 5% error to the statistical uncertainty in quadrature. To scrutinize the cooling effects on the  $L_X-T_{\text{vir}}$  relation, we used, as the first step, the total X-ray luminosities, i. e. without performing any correction to avoid the contribution from the cool-core region. As the second step, we made the cool-

core correction to the luminosities by excluding the contribution to the luminosity from a central region where cooling is putatively important. The size of the excluded central region was determined using the “cooling radius”,  $r_{\text{cool}}$ , defined as the radius at which the gas cooling time is 7.7 Gyr (the cooling time at radii greater than  $r_{\text{cool}}$  is longer than this time scale). For comparison, we also considered excluding a region of radius a fixed fraction of the virial radius, known as the “core radius”,  $r_{\text{core}}$ .

Luminosities within the cooling radius,  $L_{X,\text{rcool}}$ , were determined using CIAO 4.2 and CALDB 4.3.0. and the CIAO tool *specextract*. For each cluster with  $r_{\text{cool}} > 0$ , spectra were extracted from within the cooling radius for each ObsID in which the entire aperture fit on a single CCD. Blank sky backgrounds and weighted response functions were used, and each spectrum was binned by 25 counts per bin. Spectra for each cluster were simultaneously fit in XSPEC using a wabs\*APEC spectral model over the range (0.3 to 10.0) keV, and allowing the temperature, abundance, and normalization to vary. The hydrogen absorbing column densities were fixed to the values used for the H10 study, which were in turn taken, except in a few cases, from the Leiden/Argentine/Bonn HI Survey (Kalberla et al. 2005). The best-fitting model parameters were used with the XSPEC ‘*dummyrsp*’ command to provide unabsorbed  $L_{X,\text{rcool}}$  within the energy range (0.01 to 40) keV.

For four of the clusters (A0262, NGC4636, A3526, and NGC5044), the cooling radius proved to be larger than a single chip. In those cases, spectra were extracted from neighboring chips and fit simultaneously, tying the temperatures and abundances together but allowing the normalizations to vary separately. When neighboring chips were too small to contain a complete annulus,  $L_X$  within the total annulus was estimated using simple geometric arguments. Note that  $T_{\text{vir}}$  and  $L_{X,\text{rcool}}$  were taken from H10, wherein the X-ray data acquired with *Chandra* were calibrated and analysed using CIAO 3.2.2 and CALDB 3.0. To confirm consistency between the different versions of CIAO and CALDB, we compared values of  $L_{X,\text{core}}$  and  $L_{X,\text{rcool}}$  in cases where  $0.048R_{500} \approx r_{\text{cool}}$  and found that they agreed to within their  $1\sigma$  errors. The various X-ray quantities used for this paper are listed in Table 3.

### 3. $L_X-T_{\text{vir}}$ scaling relation

The main purpose of this investigation is to assess the effects of different physical mechanisms on the ICM properties. In particular, we wish to distinguish the roles of cooling activity and AGN heating on the  $L_X-T_{\text{vir}}$  relation. Shown in Figure 1 is  $L_X$  versus  $T_{\text{vir}}$ . At first glance, it appears that clusters with a central radio source (filled symbols) have a systematically higher X-ray luminosity than those without (open symbols). This would be rather surprising since AGN heating is believed to heat the X-ray emitting gas resulting in an opposite effect, namely, an increase in entropy and suppression of the X-ray luminosity. A more thorough analysis presented below reveals that it is the cooling of the intracluster gas in the cores of clusters, many of which harbour an AGN at their centres, that results in an enhancement in the X-ray luminosity.

To examine the effects of AGN heating and ICM cooling on the  $L_X-T_{\text{vir}}$  relation and to what extent these mechanisms are responsible for the steepening of the relation, we divided our sample into seven categories: (1) all clusters (ALL), (2) clusters with a central radio source (CRS), (3) clusters without a central radio source (NCRS), (4) SCC clusters, (5) non-strong-cool-core (NSCC=WCC+NCC) clusters, (6) WCC clusters, and (7) NCC clusters. We used the BCES (bivariate correlated errors and intrinsic scatter) fitting routine by Akritas & Bershady (1996) to determine the best-fit relations for all the categories, individually. The BCES algorithm generates four different kinds of fits, amongst which we use the ‘bisector’ method throughout this paper. This produces a line that bisects the best-fit regression lines, BCES( $X_1/X_2$ ) and BCES( $X_2/X_1$ ), where BCES( $X_1/X_2$ ) minimizes the residuals in  $X_1$  and BCES( $X_2/X_1$ ) minimizes the residuals in  $X_2$ . The bisector method ensures that both the quantities,  $L_X$  and  $T_{\text{vir}}$ , are treated symmetrically, without having to specify independent (explanatory) and dependent (response) variables. The best-fit lines are shown in Figure 1. We use a power-law functional form to indicate the  $L_X-T_{\text{vir}}$  relation [ $\frac{L_X}{10^{44} h_{71}^2 \text{ erg/s}} = \alpha \times \left(\frac{T_{\text{vir}}}{4 \text{ keV}}\right)^\beta$ ] and perform the fittings in the ln-space. The best-fit model parameters are given in Table 1(a).

The raw scatter (statistical plus intrinsic) was determined from the weighted sample variance in the  $\lg - \lg$  plane<sup>2</sup> (Arnaud et al. 2005)

$$\sigma_{\text{raw}, L_X}^2 = C_{L_X} \sum_{i=1}^N \frac{1}{\sigma_{i, L_X}^2} [Y_i - (\lg \alpha + \beta X_i)]^2$$

$$C_{L_X} = \frac{1}{(N-2)} \frac{N}{\sum_{i=1}^N (1/\sigma_{i, L_X}^2)} \quad (1)$$

$$\sigma_{\text{raw}, T_{\text{vir}}}^2 = C_{T_{\text{vir}}} \sum_{i=1}^N \frac{1}{\sigma_{i, T_{\text{vir}}}^2} [X_i - (Y_i - \lg \alpha)/\beta]^2$$

$$C_{T_{\text{vir}}} = \frac{1}{(N-2)} \frac{N}{\sum_{i=1}^N (1/\sigma_{i, T_{\text{vir}}}^2)}, \quad (2)$$

where  $Y_i = \lg(L_{X,i})$ ,  $X_i = \lg(T_{\text{vir},i})$ ,  $\sigma_{i, L_X}^2 = (\Delta Y_i)^2 + \beta^2(\Delta X_i)^2$ ,  $\sigma_{i, T_{\text{vir}}}^2 = (\Delta X_i)^2 + (\Delta Y_i)^2/\beta^2$ , and  $N$  is the sample size. The statistical scatter,  $\sigma_{\text{stat}}$ , caused by measurement errors, was estimated by taking the root-mean-square of  $\sigma_i$ . The intrinsic scatter was calculated as the difference between the raw and the statistical scatters in quadrature. In Table 1(a), we provide the intrinsic and statistical scatters in percentages ( $\sigma * \ln(10) * 100$ ) in both,  $L_X$  as well as  $T_{\text{vir}}$ . Since the statistical and intrinsic scatters add in quadrature, the contribution of the statistical errors to the total dispersion is small.

#### 3.1. Cooling against heating

The best-fit slope of the luminosity-temperature relation for the complete HIFLUGCS sample (category ‘ALL’) is  $2.94 \pm 0.16$ , which is much steeper than the self-similar value of 2.0. This result agrees with several previous works such as Arnaud &

<sup>2</sup>  $\lg(x) = \log_{10}(x)$  and  $\ln(x) = \log_e(x)$

**Table 1.** The best-fit bolometric  $L_X-T_{\text{vir}}$  relation, given by  $\frac{L_X}{10^{44} h_{71}^{-2} \text{erg/s}} = \alpha \times \left(\frac{T_{\text{vir}}}{4 \text{keV}}\right)^\beta$ , for the individual subcategories of the HIFLUGCS sample of galaxy clusters.

Category	#	$\alpha$	$\beta$	$\sigma_{\text{int}, L_X}$ (in %)	$\sigma_{\text{stat}, L_X}$ (in %)	$\sigma_{\text{int}, T_{\text{vir}}}$ (in %)	$\sigma_{\text{stat}, T_{\text{vir}}}$ (in %)
(a)	Total luminosities						
ALL	64	$2.64 \pm 0.20$	$2.94 \pm 0.16$	45.4	11.8	15.5	4.0
CRS	49	$3.04 \pm 0.23$	$3.17 \pm 0.15$	46.5	12.7	14.6	4.0
NCRS	15	$2.00 \pm 0.35$	$2.54 \pm 0.27$	59.4	10.3	23.4	4.0
SCC	28	$3.82 \pm 0.38$	$3.33 \pm 0.15$	51.8	13.1	15.6	3.9
*NSCC	36	$2.19 \pm 0.17$	$2.70 \pm 0.19$	47.4	11.1	17.5	4.1
WCC	18	$2.30 \pm 0.20$	$3.25 \pm 0.32$	34.8	12.3	10.7	3.8
NCC	18	$2.10 \pm 0.26$	$2.42 \pm 0.21$	50.4	10.8	20.8	4.5
(b)	Cool-core corrected luminosities (using the cooling radius, $r_{\text{cool}}$ , see Section 4)						
ALL	64	$1.88 \pm 0.11$	$3.05 \pm 0.14$	39.1	12.5	12.8	4.1
SCC	28	$2.00 \pm 0.16$	$3.27 \pm 0.15$	34.2	13.6	10.4	4.2
*NSCC	36	$2.01 \pm 0.15$	$2.70 \pm 0.18$	47.9	11.2	17.7	4.1
WCC	18	$1.95 \pm 0.15$	$3.20 \pm 0.29$	36.3	12.4	11.4	3.9
*CC	46	$1.97 \pm 0.11$	$3.25 \pm 0.13$	33.2	13.0	10.2	4.0

\* CC = SCC+WCC, NSCC = WCC+NCC

Evrard (1999), Allen & Fabian (1998), Novicki et al. (2002), and Zhang et al. (2007). After the subdivision into different classes, several interesting features are evident. A comparison of slopes shows that the SCC clusters have the steepest relation ( $\beta = 3.33 \pm 0.15$ ), whereas the NCC clusters have the shallowest ( $\beta = 2.42 \pm 0.21$ ). Note that the high power-law index for SCCs is not due to selection effects. Even though it is true that there is not even a single NCC with  $T_{\text{vir}} < 2.5 \text{ keV}$ , the steep  $L_X - T_{\text{vir}}$  relation for SCCs is a generic feature of clusters with a short central cooling time. This can be easily verified by eliminating from the SCC subsample all clusters with  $T_{\text{vir}} < 2.5 \text{ keV}$  (eight in number) and fitting the data again. After doing this, we find that  $\beta = 3.14 \pm 0.34$ , which is consistent with the power-law index obtained for the complete SCC sample, and still much higher than the fitted power-law index for the NCC subsample.

A similar contrast in slopes is true for the CRS and NCNS clusters. The fits for CRS and SCC clusters have consistent slopes within the errorbars, and, likewise, the fits for NCNS and NCC clusters have consistent slopes within the errorbars (although the CRS and SCC cluster subsamples have different normalizations, the SCC clusters being systematically higher in luminosity than the CRS clusters). This is not unsurprising since we know from M09 that the probability of finding a central radio source in a cluster is an increasing function of the cooling strength, with SCC clusters having the highest incidence (100%) and the NCC clusters having the lowest incidence (44%). Hence, the fit through the CRS cluster subsample is dominated by the SCC clusters and, similarly, the fit through the NCNS cluster subsample is dominated by the NCC clusters.

In Figure 2, we present the lg-space residuals in  $L_X$  for each category based on its respective best-fit. Figure 2(b) indicates that the CRS subsample actually comprises clusters from two different populations rather than one. CRS clusters with a strong cool core (filled boxes) are clearly above the zero-deviation line (18 out of 28), whereas those without (circles and triangles) are on-average below (15 out of 21). Using the

Kolmogorov-Smirnov (K-S) test, we find that the probability of the null hypothesis, i.e. that the two samples (CRS clusters with and without a SCC) are drawn from the same underlying population, is only 1.2%. A similar, though less dramatic, segregation is seen between NSCC clusters with a CRS, represented by the filled symbols in Figure 2(e) and those without a CRS, represented by the open symbols in Figure 2(e). Fourteen of the 21 NSCC clusters with a CRS lie above the zero-deviation line and 6 out of 15 NSCC clusters without a CRS lie above the zero-deviation line. The K-S probability of the null hypothesis is 7%. NSCC clusters with a CRS are still biased towards positive deviation. This is likely because a higher fraction of WCC clusters have a CRS than the NCC, once again implying that the cooling activity dictates the overall trend. The NCC category in Figure 2(g), even though low in sample size, most clearly illustrates this argument. Both the subsamples, the NCC clusters with (filled symbols) and without (open symbols) a CRS, can be seen equally distributed about the zero-deviation line. Four of the 8 NCC clusters with a CRS lie above the zero-deviation line and 7 out of 10 NCC clusters without a CRS lie above the zero-deviation line. The K-S probability that the NCC clusters with and without a CRS originate from a single population is 54%. In other words, subsamples marked by the absence (or presence) of cooling may be visualized as originating from a single population. That the subsamples having identical cooling properties seem to follow the same  $L_X-T_{\text{vir}}$  relation, independent of the presence of a radio source, implies that it is the cooling of the intracluster gas that plays a more dominant role in influencing the  $L_X-T_{\text{vir}}$  relation rather than the AGN activity.

We conclude that on the high-mass scale ( $T_{\text{vir}} > 2.5 \text{ keV}$ ) the steepening of the  $L_X-T_{\text{vir}}$  relation is primarily related to the cooling of the ICM. This is clearly manifested by the  $L_X-T_{\text{vir}}$  relation being the steepest for the SCC clusters. As the forthcoming analysis shows, the cooling effects in CCs leading to the steeper relation are likely distributed over a region

larger than that described by the cooling radius. The cut at  $T_{\text{vir}} = 2.5$  keV is motivated by the SCC and NCC fits crossing at  $\lg(kT_{\text{vir}}) \sim 0.4$  (see Figure 1). As discussed in Section 6, it is most likely that both ICM cooling and AGN heating have to be considered in describing the  $L_{\text{X}} - T_{\text{vir}}$  relation. However, owing to the nature of the sample containing mostly high-mass clusters, we see direct evidence of only the former.

#### 4. Cool-core contribution to the X-ray luminosity and scatter in the $L_{\text{X}} - T_{\text{vir}}$ relation

It has often been noted that excluding cool-core clusters decreases the overall intrinsic dispersion in the  $L_{\text{X}} - T_{\text{vir}}$  relation (O’Hara et al. 2006; Pratt et al. 2009; Chen et al. 2007), with the direct implication that the cool-core related activities are the prime contributors to the observed scatter. Our observations do not completely support this conclusion. Qualitatively, this may be seen by noting that, firstly, if that were true, the intrinsic scatter for the subgroup ‘NSCC’ containing no strong cool-core clusters would have to be significantly lower than that corresponding to the ‘ALL’ category. From Table 1(a) it can be seen this is not the case. Secondly, the subgroup ‘NCRS’, which comprises predominantly NCC clusters and not a single SCC cluster has the largest intrinsic dispersion in both X-ray luminosity (59.4%) as well as virial temperature (23.4%). Also, the ‘NCC’ subgroup has a large a high intrinsic scatter (50.4 %), comparable to the ‘SCC’ subgroup (51.8%). That these two subsamples have comparable scatters implies that one cannot impute the scatter obtained for the ‘ALL’ category to only the process of intracluster-medium cooling. In H10, it was found that most of the NCC clusters in the *HIFLUGCS* sample show signs of merger activity, a process that entails shock heating and adiabatic compression and may cause the system to deviate from a given  $L_{\text{X}} - T_{\text{vir}}$  relation.

In the following, we quantify the degree to which the cooling activity contributes to the observed scatter about the  $L_{\text{X}} - T_{\text{vir}}$  relation. To calculate the X-ray luminosity originating from the cool cores of the clusters, the “cool-core luminosity”, we choose two defining regions. The first region is the “cooling radius”,  $r_{\text{cool}}$ , the radius at which the cooling time of the gas is 7.7 Gyr. The NCCs by definition have  $r_{\text{cool}} = 0$ . The average cooling radius of the remaining 46 cool-core (CC) clusters (SCCs+WCCs) is  $\sim (0.07 \pm 0.03)R_{500}$ . The second region is the “core radius”,  $r_{\text{core}} = 0.048R_{500}$  (H10, unpublished), a fixed fraction of the virial radius. The cool-core luminosities (0.01-40) keV from  $r_{\text{cool}}$  and  $r_{\text{core}}$  versus temperature are shown in the upper left and right panels of Fig. 3, respectively. The left panel shows those SCCs and WCCs with a non-zero  $r_{\text{cool}}$ , whereas the right panel shows all the 64 clusters. Even though  $r_{\text{core}}$  closely matches the average cooling radius ( $\sim 0.05R_{500}$ ) over all 64 clusters,  $r_{\text{cool}}$  is likely a better parameter to assess the scatter due to cooling in the  $L_{\text{X}} - T_{\text{vir}}$  relation.  $r_{\text{core}}$  shows a relatively smaller scatter with temperature than  $r_{\text{cool}}$ . However, this is not surprising. The core radius corresponds to a fixed fraction of a characteristic overdensity scale, whereas the cooling radius varies from cluster to cluster and its scaling relative to the  $R_{500}$  has a large dispersion (see Fig. 4). Since the cooling radius is closely tied to the cooling process, it is precisely

this dispersion that may be adding to the scatter in the  $L_{\text{X}} - T_{\text{vir}}$  relation. For samples where detailed density and temperature profiles cannot be obtained (such as those containing high- $z$  clusters) for the precise determination of  $r_{\text{cool}}$ , we propose that a cut equal to the average cooling radius  $\sim 0.07R_{500}$  be used for the cool-core correction. A cut larger than this is likely to overestimate the fraction of the luminosity generated by cooling.

We calculate the fraction of the X-ray luminosity originating from the cooling radius as  $f_{L_{\text{X},\text{cool}}} = L_{\text{X},\text{cool}}/L_{\text{X}}$ , and that originating from the core radius as  $f_{L_{\text{X},\text{core}}} = L_{\text{X},\text{core}}/L_{\text{X}}$ , where  $L_{\text{X},\text{cool}}$  and  $L_{\text{X},\text{core}}$  are the integrated luminosities over  $r_{\text{cool}}$  and  $r_{\text{core}}$ , respectively. We find that the  $f_{L_{\text{X},\text{cool}}}$  for the SCCs is equal to  $44.0\% \pm 14.2\%$ , for the WCC is equal to  $15.2\% \pm 15.5\%$ , for the SCCs and WCCs combined is equal to  $31.4\% \pm 31.6\%$ , and for all the 64 clusters is  $23.5\% \pm 23.5\%$  (the  $1\sigma$  error in  $f_{L_{\text{X},\text{cool}}}$  is greater than the mean for some of the subsets and reflects non-gaussianity in  $f_{L_{\text{X},\text{cool}}}$ ). Similarly, the  $f_{L_{\text{X},\text{core}}}$  for the whole sample is equal to  $17.8\% \pm 13.1\%$ . Hence, the variation in total  $L_{\text{X}}$  due to the variation in  $L_{\text{X},\text{cool}}$  for the whole sample (23.5%) is much higher than that due to the variation in  $L_{\text{X},\text{core}}$  (13.1%). These variations may be directly compared to the percentage scatter in  $L_{\text{X}}$  determined for the ‘ALL’  $L_{\text{X}} - T_{\text{vir}}$  relation (45.4%). The contribution of the cooling activity to the scatter in the  $L_{\text{X}} - T_{\text{vir}}$  relation is  $(23.5\%/45.4\%)^2 \sim 27\%$  if the cooling radius is considered and  $(13.1\%/45.4\%)^2 < 9\%$  if the core radius is considered (note that the contributions to the scatter add in quadrature). However, as mentioned above, we deem that the region described by the cooling radius is a more appropriate region to use to assess the luminosity due to cooling and its contribution to the scatter. Hence, this implies that we can expect about 25% of the scatter in the  $L_{\text{X}} - T_{\text{vir}}$  relation to result from the cluster-to-cluster variation in the central luminosities of CC clusters. The scatter expected after excluding the cool-core luminosity is  $45.4\% \sqrt{1.0 - (23.5\%/45.4\%)^2} \sim 39\%$ .

In the lower left panel of Fig. 3, we show the total X-ray luminosity versus temperature and in the lower right panel of Fig. 3 the cool-core excised total luminosity versus the virial temperature. We determine the  $L_{\text{X}} - T_{\text{vir}}$  relation after excluding the cooling luminosity and find

$$\frac{L_{\text{X}}}{10^{44} \text{ erg/s}} = (1.88 \pm 0.11) \times \left( \frac{T_{\text{vir}}}{4 \text{ keV}} \right)^{3.05 \pm 0.14}. \quad \text{The exclusion of the core emission does not affect the slope of the } L_{\text{X}} - T_{\text{vir}} \text{ relation and is consistent with that corresponding to the ‘ALL’ category including the core } (2.94 \pm 0.16). \text{ However, it does produce a smaller normalization and a shallower slope for the SCCs, such that the SCCs and WCCs are now indistinguishable and have the same } L_{\text{X}} - T_{\text{vir}} \text{ parameters. The best-fit } L_{\text{X}} - T_{\text{vir}} \text{ parameters for the subsets after the cool-core correction, i. e. after subtracting } L_{\text{X},\text{cool}} \text{ from the total luminosities, are given in Table 1(b). Since no correction was made for the NCCs, the } L_{\text{X}} - T_{\text{vir}} \text{ parameters and the scatters in the luminosity and temperature for the NCC subset remain the same. The intrinsic dispersion about the } L_{\text{X}} - T_{\text{vir}} \text{ relation for ‘ALL’ clusters obtained after the cool-core correction is } 39.1\%. \text{ This is in very good agreement with the scatter expected after excising the cooling luminosity based on the dispersion in } f_{L_{\text{X},\text{cool}}}, \text{ as proposed above. In other words, about } 27\% \text{ of the scatter in the } L_{\text{X}} - T_{\text{vir}} \text{ relation may be attributed to the luminos-}$$

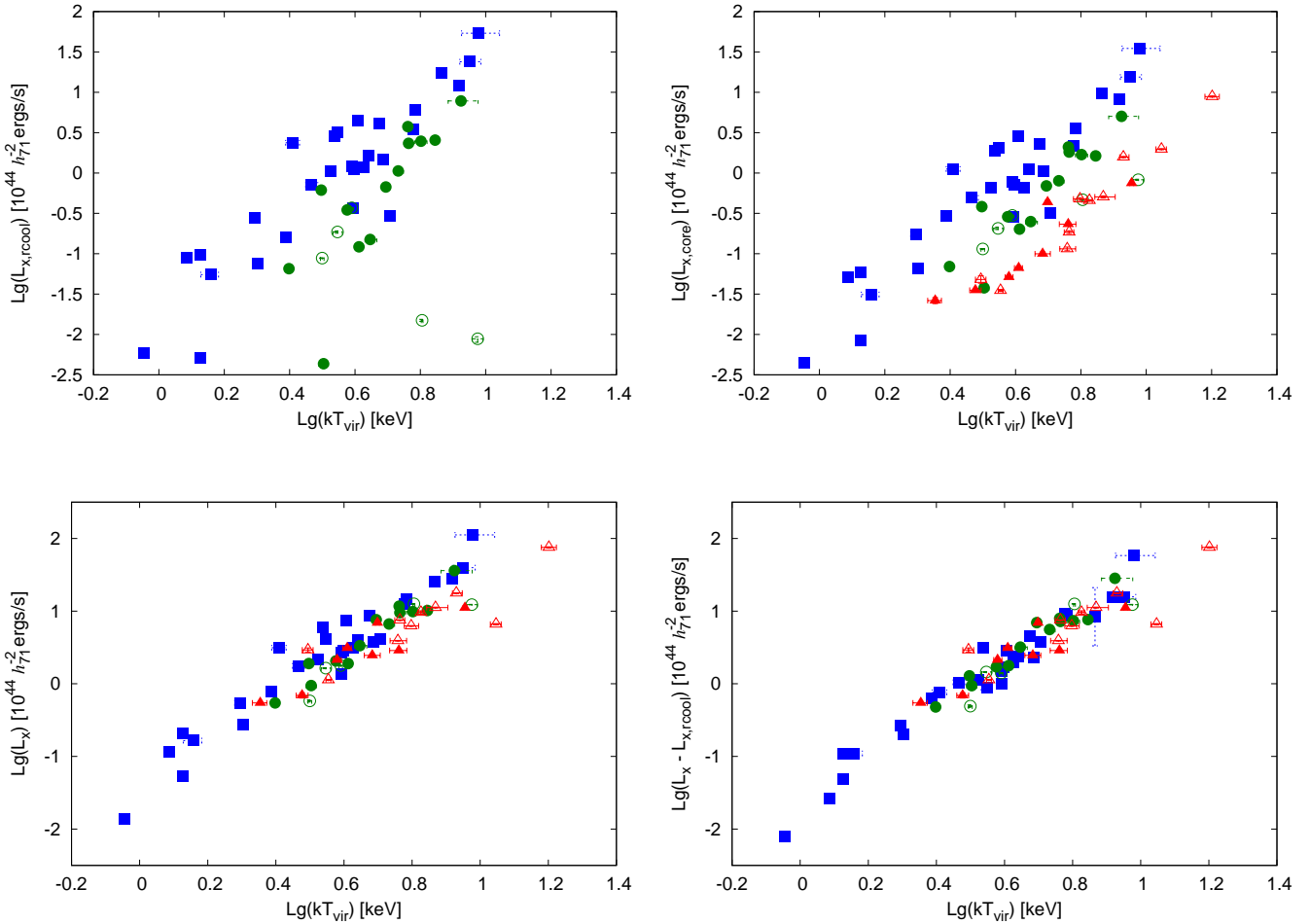


**Fig. 3.** *Upper panel:* The X-ray luminosity within the cooling radius at which the cooling time equals 7.7 Gyr,  $L_{X,\text{cool}}$  (left), and that within the core radius of 4.8%  $R_{500}$ ,  $L_{X,\text{core}}$  (right), vs temperature. *Lower panel:* The total X-ray luminosity vs temperature (left) and the total X-ray luminosity minus  $L_{X,\text{cool}}$  vs temperature (right). Shown are the three categories – strong cool-core (SCC), weak cool-core (WCC) and non-cool-core (NCC) clusters. The symbol representation is the same as in Fig. 1.

ity within  $r_{\text{cool}}$ . However, *after* the cool-core correction, the CC (SCC+WCC) subset shows the least scatter in luminosity (33.2%), followed by the SCC subset (34.2%). Hence, the remaining scatter in the  $L_X - T_{\text{vir}}$  relation after excising  $r_{\text{cool}}$  from the SCCs and WCCs is largely due to the NCCs (50.4%).

We expect the scatter to continually decrease with the size of the excised region since the effects of cooling and heating are expected to dampen with increasing clustercentric distance. This is consistent with the findings of Pratt et al. (2009), who excised the 15% $R_{500}$  region and found a reduction in scatter by more than 50%. We do not conduct the above analysis with 15% $R_{500}$ ; the reasons are twofold. Firstly, because of the limited field-of-view of *Chandra*, more and more emission falls out of the observed field with increasing radius (especially for the nearby clusters), forcing us to make assumptions about the missing emission. This defeats the purpose of obtaining precise luminosity measurements to minimize the scatter. Secondly, as seen with the 4.8% $R_{500}$  core region above, excising a fixed fraction

of the virial radius is not always meaningful. The actual cooling region scaled by  $R_{500}$  contributing to the scatter varies from cluster to cluster.

Note that in the AGN-regulated feedback paradigm, AGN heating must occur over the same scale as the cooling in order to balance it. While this analysis shows that excluding the cooling region in the cool-core clusters reduces the scatter in the  $L_X - T_{\text{vir}}$  relation, we cannot comment on how much of the scatter from the excised region is caused by cooling activity and how much by AGN heating. For a given temperature, not only might the SCC clusters have a higher luminosity than NCCs, but for a given luminosity either the SCC clusters might have lower virial temperatures and/or the NCC clusters higher virial temperatures. In their simulations, Burns et al. (2008) indeed find an abundance of cool gas in the region 0.05 $R_{500}$  to 0.3 $R_{500}$ , i. e. beyond the cores of CC clusters. This could result in an overall lower virial temperature in SCC clusters. As noted previously (Section 4), most NCC clusters in our sample

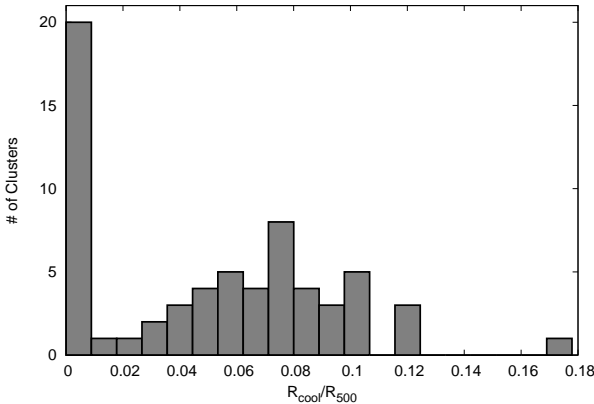


**Fig. 4.** A histogram of the scaled cooling radius,  $r_{\text{cool}}/R_{500}$ , showing a large dispersion. There are 18 non-cool-core clusters with  $r_{\text{cool}} = 0$  and 46 cool-core clusters with an average cooling radius of  $(0.07 \pm 0.03)R_{500}$ .

are merger systems, which due to heating may have a higher virial temperature.

Lastly, we point out that the subgroup of WCC clusters displays the least scatter (34.8%). This is perhaps not so surprising because these are clusters that neither possess a strong cool-core nor exhibit any indication of an ongoing or past major merger (Hudson et al. 2010). We note that the SCCs and WCCs have statistically consistent slopes and so it may be that WCCs are actually progenitors of the SCC clusters, whose cool cores would eventually grow in time to match those of SCC clusters.

## 5. Systematics

### 5.1. Selection effects

Flux-limited samples suffer from the well-known Malmquist bias, namely that brighter objects have a higher detection rate than fainter objects. This bias may affect the observed fractions of SCC, WCC, and NCC clusters, and, in addition, the fitted  $L_X-T_{\text{vir}}$  relations.

Owing to their enhanced central X-ray-emission, strong cool-core clusters have a higher chance of detection and this may explain the observed higher fraction of SCC clusters in flux- and luminosity-limited samples. Since we have a complete flux-limited sample, we can estimate the magnitude of this bias. We simulated samples of clusters, which follow the X-ray temperature function (XTF) given by  $dN/dV \sim T^{-3.2}$  (Markevitch 1998), in the temperature range (0.5–20) keV and redshift range from 0.001 to 0.25 [the XTF used is an approximation; a more realistic functional form consists of a power-law and an exponential high temperature cut-off (e.g. Henry 2000; Ikebe et al. 2002)]. In H10, it is shown that SCC, WCC, and NCC clusters come from the same parent redshift distributions within a  $1\sigma$  standard deviation. Hence, we assigned random redshifts to clusters conforming to the  $N \propto D^3$  law, where  $D$  is the proper distance. We assigned clusters to be SCC,

WCC, and NCC clusters according to certain input fractions, which were varied in the overall process. The luminosities of the SCC, WCC, and NCC clusters were calculated using the  $L_X-T_{\text{vir}}$  relation corresponding to each category as determined in Section 3.1.

To estimate the effect of applying a flux-limit to a mixed sample of SCCs, WCCs, and NCCs, we applied the *HIFLUGCS* flux-limit,  $f_X$  (0.1 – 2.4) keV  $\geq 2 \times 10^{-11}$  erg s $^{-1}$  cm $^{-2}$ , to the simulated sample and reprojected the fluxes to the  $L_X-T_{\text{vir}}$  plane. We tried four different cases. In the first (simplest) case, we assumed that the SCCs, WCCs and NCCs have the same slope (3.33) and fixed the normalizations to those found from the fits to the data (Table 1)(a). In the second case, we fixed the slopes for SCCs, WCCs and NCCs to the fitted values. In the third case, we also inserted the intrinsic scatter [from Table 1(a)] about the fitted  $L_X-T_{\text{vir}}$  relations in X-ray luminosity. In all three cases, we varied the input fractions to determine the values that best matched the observed fractions. The addition of scatter about the  $L_X-T_{\text{vir}}$  relations has an effect, as expected, only on the normalizations. The data points scattered to higher values have a higher likelihood of falling above the flux-limit, thereby increasing the normalization in all three cases. In the fourth case, we fixed the fractions of SCC, WCC, and NCC to the best-fit values from the third case and varied the normalizations to determine the ‘true’ values, which yielded the observed normalizations. The results of these simulations are given in Table 2. The two main results are that (1) the SCC input fraction is on average about 25% lower than the observed value and (2) the inclusion of scatter increases the normalization of all the three  $L_X-T_{\text{vir}}$  relations, the true normalizations being about 12%, 7%, and 17% lower than the observed values for SCC, WCC, and NCC clusters, respectively.

### 5.2. Chandra calibration

The virial temperature acquired with *Chandra* that were used to determine the overall  $L_X-T_{\text{vir}}$  relation for the *HIFLUGCS* sample were calibrated and analysed using CIAO 3.2.2 and CALDB 3.0 (Hudson et al. 2010). In the meantime, a new version of the *Chandra* calibration package, CALDB 4.1.1, has been made available as of January 2009. In this section, we give a brief comparison between the results obtained using the old and the new CALDB packages.

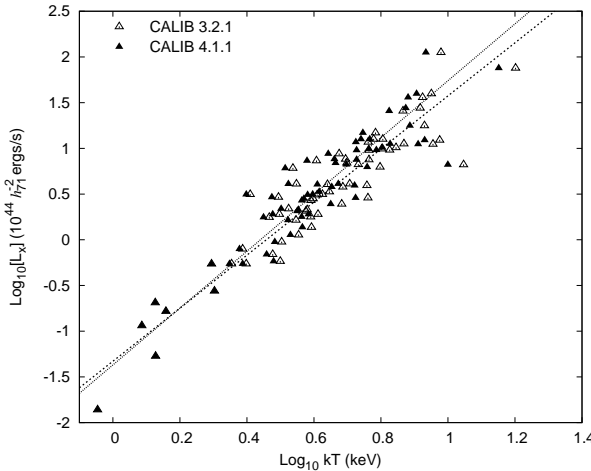
The *Chandra*–*XMM-Newton* cross calibration project with the International Astronomical Consortium for High Energy Calibration (IACHEC<sup>3</sup>) resolved a disagreement between the two instruments to a certain extent. Internal consistency checks showed that the *Chandra*–ACIS derived temperatures for clusters hotter than 4 keV were systematically higher than the *XMM-Newton*–EPIC derived ones. This may result in an erroneous slope estimate of the  $L_X-T_{\text{vir}}$  relation.

Minor adjustments to the effective area of the HRMA (High Resolution Mirror Assembly) have now been incorporated in CALDB 4.1.1, which are based on the predictions of the new model that corrects for a hydrocarbon contamination layer. We

<sup>3</sup> <http://www.iachec.org/index.html>

**Table 2.** The impact of selection effects on the observed fractions of SCCs, WCCs, and NCCs and the  $L_X-T_{\text{vir}}$  relations.

Case	Category	Input Fractions	Output Fractions	Input $L_X-T_{\text{vir}}$ relations $\alpha, \beta$	Output $L_X-T_{\text{vir}}$ relations $\alpha, \beta$
No scatter, observed $\alpha, \beta$ fixed to 3.33	SCC	0.310	$0.432 \pm 0.040$	3.82, 3.33	3.82, 3.33
	WCC	0.335	$0.286 \pm 0.038$	2.30, 3.33	2.30, 3.33
	NCC	0.355	$0.282 \pm 0.039$	2.10, 3.33	2.10, 3.33
No scatter, observed $\alpha$ and $\beta$	SCC	0.340	$0.437 \pm 0.040$	3.82, 3.33	3.82, 3.33
	WCC	0.350	$0.276 \pm 0.034$	2.30, 3.25	2.30, 3.25
	NCC	0.310	$0.287 \pm 0.038$	2.10, 2.42	2.12, 2.42
Scatter included, observed $\alpha$ and $\beta$	SCC	0.340	$0.438 \pm 0.038$	3.82, 3.33	$4.31 \pm 0.08, 3.35 \pm 0.01$
	WCC	0.355	$0.281 \pm 0.037$	2.30, 3.25	$2.43 \pm 0.02, 3.27 \pm 0.01$
	NCC	0.305	$0.281 \pm 0.038$	2.10, 2.42	$2.56 \pm 0.07, 2.51 \pm 0.01$
Scatter included, observed $\beta$	SCC	0.340	$0.432 \pm 0.042$	3.40, 3.33	$3.85 \pm 0.06, 3.35 \pm 0.01$
	WCC	0.355	$0.291 \pm 0.038$	2.15, 3.25	$2.30 \pm 0.02, 3.27 \pm 0.01$
	NCC	0.305	$0.277 \pm 0.042$	1.75, 2.42	$2.13 \pm 0.05, 2.51 \pm 0.01$

**Fig. 5.** The effect of new *Chandra* calibration CALDB 4.1.1. on the  $L_X-T_{\text{vir}}$  relation.

used the results of the comparison between cluster temperatures derived for the *XMM-Newton* and *Chandra* data, using the two measurements of HRMA effective area (David 2009, figure 21). We determined the best-fit lines to establish the relation between the ACIS temperatures,  $T_{3.2.1}$  and  $T_{4.1.1}$ , in the energy band 0.5 keV to 7.0 keV, corresponding to the two *Chandra* calibration schemes, CALDB 3.2.1 and CALDB 4.1.1. This relation is given by

$$T_{4.1.1} = 0.875 * T_{3.2.1} + 0.251, \quad (3)$$

where the temperatures are in units of keV. Using this relation, we calculated  $T_{4.1.1}$  for each cluster with  $T_{3.2.1} > 2$  keV. The old and the new temperature estimates are shown in Figure 5. The slope of the best-fit through the new data points ('ALL') obtained from the BCES algorithm is  $3.11 \pm 0.16$ , and is consistent within the errorbars with the previous one given in Table 1(a). Thus, we conclude that our best-fit estimates of the  $L_X-T_{\text{vir}}$  relation for the different categories obtained using CALDB 3.1.2 are not affected by the new *Chandra* calibration.

## 6. Discussion

The  $L_X-T_{\text{vir}}$  relation in clusters has been studied extensively by several other groups (e.g. O'Hara et al. 2006; Puchwein et al. 2008; Poole et al. 2007; Jetha et al. 2007) to examine the intricate processes operating in the ICM that need to be well-understood before using X-ray observations of clusters to constrain cosmological parameters. Most observational studies focus either on intracluster cooling or AGN heating as the cause of the deviation of the  $L_X-T_{\text{vir}}$  relation from self-similar form of the relation. Our multi-wavelength coverage of the topic allows us to unravel the effects of both mechanisms, simultaneously.

The general conclusion of previous studies of the AGN effects on the state of the intracluster gas is that AGN heating removes gas from the centres of halos (Sijacki & Springel 2006; Puchwein et al. 2008; Croston et al. 2005; Short & Thomas 2009). For example, in the model of Short & Thomas (2009), the mechanical heating associated with expanding jets and lobes produced by the central engine with radio-mode accretion pushes the gas away from the centre to the outer regions. This has the effect of reducing the density of the X-ray emitting gas in the halo cores. AGN-heating is especially effective in poor clusters and groups because of their shallow gravitational potential wells. In contrast, cooling increases the gas density at the centre and causes the X-ray luminosity of the cluster cores to increase. The two processes therefore have opposite effects on the X-ray luminosity.

These results can be reconciled quite well with our findings. Even though our observations lend support only to the impact of cooling, we propose that both the mechanisms have a significant influence on the  $L_X-T_{\text{vir}}$  relation but on different scales. While we have shown that ICM cooling dominates the deviation of the  $L_X-T_{\text{vir}}$  relation from its norm in high-mass systems, we speculate that AGN heating dominates the state of the intracluster gas in low-mass systems. Owing to the radiative cooling of the ICM, we observe that the high-mass SCC clusters in our sample ( $T_{\text{vir}} > 2.5$  keV) have a higher luminosity than the high-mass NCC clusters. The low-mass clusters ( $T_{\text{vir}} < 2.5$  keV) with AGN are predicted to display the reverse

trend. AGN heating in these systems becomes more dominant and causes the X-ray luminosity to decrease relative to systems without any source of heating. This is yet to be checked with a statistically complete sample of low-mass clusters and groups. Our sample has only ten low-mass clusters with  $T_{\text{vir}} < 2.5 \text{ keV}$ , out of which eight have strong cool-cores; low statistics of NSCC clusters makes it difficult to test this scenario. However, this is in line with the results obtained by Croston et al. (2005). They analysed a subsample of groups from the *GEMS* group sample (Group Evolution Multiwavelength Study, Osmond & Ponman 2004) and found that the radio-loud groups lie on a steeper  $L_X - T_{\text{vir}}$  relation. Their analysis, however, supports a model whereby AGN heating, instead of the displacement of gas and the consequential decrement in the X-ray luminosity, results in the deposition of the kinetic energy of the radio source in the form of thermal energy, causing the gas temperature to increase. Irrespective, we propose that it is the combination of both of the processes, AGN heating and ICM cooling, that causes the steepening of the  $L_X - T_{\text{vir}}$  relation.

Our results, however, seem to contradict the simulations of Sijacki & Springel (2006). Besides self-gravity, their recipe includes radiative cooling, photoionization, star-formation, supernovae heating, and AGN-heating in the form of hot, radio-plasma filled bubbles. According to their results, the effect of bubble heating is the same for both low- and high-mass clusters and a corresponding decrement in X-ray luminosity should be seen in CRS clusters. This is incompatible within the framework of AGN-regulated feedback in cool-core systems. Cool-core halos at a given temperature, because of the nature of cooling, have an enhanced luminosity and, at the same time as shown in Mittal et al. (2009), undebatably favour AGN at their centres; *all* SCCs have a centrally located AGN. However, this does not imply that *every* SCC has an enhanced luminosity in that low-mass SCC clusters may have a decrement because of AGN heating. Whether there is a net increment (ICM cooling) or decrement (AGN heating) in luminosity depends upon the scale of the system.

After applying the cool-core correction, the CC clusters show the least intrinsic dispersion of 33%. Pratt et al. (2009) obtained a scatter of 26% using luminosity and temperature in the range (0.15 to 1) $R_{500}$ . It is certainly plausible that the scatter decreases with increasing radius of the region excluded for the cool-core correction. Even though 15% $R_{500}$  is too large a region relative to the average cooling radius of the CCs, it may be that for some of the clusters the cooling radius does not encapsulate the total volume affected by cooling. The slope of the CC clusters after the cool-core correction is indeed as steep as before (note that excluding low-mass systems with  $T_{\text{vir}} < 2.5 \text{ keV}$  does not make a difference). In the context of the  $L_X - T_{\text{vir}}$  relation, this could imply that the cooling effects are distributed over a much larger region ( $\sim 0.3R_{500}$ ) than that suggested by the cooling radius. There are 11 SCCs with higher luminosities than the NCCs after the cool-core correction. A simple calculation shows that the further decrement in the luminosity required to match the SCC and the NCC slopes is in the range 2% to 100% of  $L_{X,\text{cool}}$ , with a mean of around 35%. Hence, it is plausible that if a larger core region is subtracted for these clusters, the slope of the SCCs would flatten. We propose that

in future studies other diagnostic regions, similar to  $r_{\text{cool}}$  and  $r_{\text{core}}$ , should be investigated in order to determine the optimal region over which to make the cool-core correction.

There could be several factors contributing to the remaining scatter in the  $L_X - T_{\text{vir}}$  relation after the cool-core correction. One such factor is the pre-heating process in which supernovae, AGN, stars etc heat the gas in some early epoch of cluster formation (e.g. Kaiser 1991; Evrard & Henry 1991; Navarro et al. 1995). The concept of pre-heating is still not very well-understood, especially the exact physical processes that govern it. The non-gravitational processes associated with pre-heating are usually collectively inserted into simulations in the form of entropy. McCarthy et al. (2004) investigated integrated models containing radiative cooling and entropy injection to study the global and structural properties of galaxy clusters. Their results indicate that such models can reproduce the observed intrinsic scatter in the scaling relations, including the  $L_X - T_{\text{vir}}$  relation, although it may be that different levels of injection entropy [(100 to 500) keV cm<sup>2</sup>] are required for different mass ranges. Lastly, self-similar clusters follow  $L_X \propto f^2 T_{\text{vir}}^2 (1 + z_f)$ , where  $f$  is the gas mass fraction and  $z_f$  is the redshift of the cluster formation. Hence, different epochs of cluster formation and gas mass fraction may also contribute to the scatter at some level.

## 7. Conclusions

We have investigated the two competing physical processes that affect the  $L_X - T_{\text{vir}}$  relation in galaxy clusters using the 64 X-ray brightest halos in the sky. This is the largest statistically-complete sample with high-quality X-ray and radio data. The two competing processes in question are the cooling of the intracluster medium (ICM) and AGN heating. Our main results are as follows:

1. On cluster scales, the cooling of the intracluster medium (ICM) is the dominant of the two mechanisms that shapes the  $L_X - T_{\text{vir}}$  relation in the strong cool-core clusters. Although they each contain a central radio source, the strong cool-core clusters (SCCs) have enhanced luminosities.
2. SCC clusters with short cooling times ( $t_{\text{cool}} < 1 \text{ Gyr}$ ) have the steepest power-law index (3.33) whereas the non-cool-core (NCC) clusters with long cooling times ( $t_{\text{cool}} > 7.7 \text{ Gyr}$ ) have the shallowest power-law index (2.42).
3. The intrinsic dispersion in  $L_X$  ranges from a minimum of 34.8% for weak cool-core (WCC) clusters ( $1 \text{ Gyr} < t_{\text{cool}} < 7.7 \text{ Gyr}$ ) to maximum of 59.4% for clusters with no central radio source (NCRS).
4. Our results do not show that the SCCs only are responsible for the scatter in the  $L_X - T_{\text{vir}}$  relation. There is similar scatter for SCC (51.8%), NCC (50.4%), and NSCC (47.4%) clusters.
5. After applying the cool-core correction, the intrinsic scatter about the  $L_X - T_{\text{vir}}$  relation in luminosity decreases from 45.4% to 39.1%. The SCCs+WCCs display the least scatter after the correction (33.2%) followed by the SCCs (34.2%) and then WCCs (36.3%). The NCC subset, for which the

- scatter is unchanged (50.4%), is the dominant source of scatter in the  $L_X-T_{\text{vir}}$  relation after the cool-core correction.
6. The variation in the cool-core luminosity,  $L_X(< r_{\text{cool}})$ , where  $r_{\text{cool}}$  is the cooling radius at which  $t_{\text{cool}} = 7.7$  Gyr, contributes 27% to the total intrinsic scatter about the  $L_X-T_{\text{vir}}$  relation. The average cooling radius for SCCs+WCCs is  $(0.07 \pm 0.03)R_{500}$ .
  7. Owing to the nature of the sample (flux-limited), the actual fractions of SCC, WCC and NCC clusters may be similar. The observed fraction of SCCs is likely higher because of their relatively enhanced X-ray luminosities. The normalizations of the  $L_X-T_{\text{vir}}$  relations of SCC, WCC, and NCC clusters were individually corrected for Malmquist bias, caused by the scatter, using Monte Carlo simulations.

Our results suggest that on cluster scales, intracluster medium cooling (where relevant) is more predominant than AGN heating in the context of the  $L_X-T_{\text{vir}}$  scaling relation. Furthermore, we speculate that AGN heating becomes increasingly important as the size of the halos decreases and may be the dominant of the two processes on galaxy group scales.

*Acknowledgements.* We thank the referee for the valuable comments on the manuscript and insightful suggestions. R. M. acknowledges support from the Deutsche Forschungsgemeinschaft (DFG) through the Schwerpunkt Program 1177 (RE 1462/4) and T. H. R. acknowledges support from the DFG through the Emmy Noether and Heisenberg research grants RE 1462/2 and RE 1462/5.

## References

- Akritas, M. G. & Bershady, M. A. 1996, ApJ, 470, 706  
 Allen, S. W. & Fabian, A. C. 1998, MNRAS, 297, L57  
 Arnaud, M. & Evrard, A. E. 1999, MNRAS, 305, 631  
 Arnaud, M., Pointecouteau, E., & Pratt, G. W. 2005, A&A, 441, 893  
 Borgani, S. & Guzzo, L. 2001, Nature, 409, 39  
 Bower, R. G., McCarthy, I. G., & Benson, A. J. 2008, MNRAS, 390, 1399  
 Burns, J. O., Hallman, E. J., Gantner, B., Motl, P. M., & Norman, M. L. 2008, ApJ, 675, 1125  
 Chen, Y., Reiprich, T. H., Böhringer, H., Ikebe, Y., & Zhang, Y.-Y. 2007, A&A, 466, 805  
 Croston, J. H., Hardcastle, M. J., & Birkinshaw, M. 2005, MNRAS, 357, 279  
 David, L. 2009, Chandra News, 16, 19  
 Eke, V. R., Navarro, J. F., & Frenk, C. S. 1998, ApJ, 503, 569  
 Evrard, A. E. & Henry, J. P. 1991, ApJ, 383, 95  
 Fabian, A. C., Crawford, C. S., Edge, A. C., & Mushotzky, R. F. 1994, MNRAS, 267, 779  
 Govoni, F., Murgia, M., Markevitch, M., et al. 2009, A&A, 499, 371  
 Henry, J. P. 2000, ApJ, 534, 565  
 Hudson, D. S., Mittal, R., Reiprich, T. H., et al. 2010, A&A, 513, A37+ (H10)  
 Ikebe, Y., Reiprich, T. H., Böhringer, H., Tanaka, Y., & Kitayama, T. 2002, A&A, 383, 773  
 Jetha, N. N., Ponman, T. J., Hardcastle, M. J., & Croston, J. H. 2007, MNRAS, 376, 193  
 Kaiser, N. 1986, MNRAS, 222, 323  
 —. 1991, ApJ, 383, 104  
 Kalberla, P. M. W., Burton, W. B., Hartmann, D., et al. 2005, A&A, 440, 775  
 Leauthaud, A., Finoguenov, A., Kneib, J., et al. 2010, ApJ, 709, 97  
 Magliocchetti, M. & Brüggen, M. 2007, MNRAS, 379, 260  
 Mantz, A., Allen, S. W., Ebeling, H., & Rapetti, D. 2008, MNRAS, 387, 1179  
 Markevitch, M. 1998, ApJ, 504, 27  
 McCarthy, I. G., Balogh, M. L., Babul, A., Poole, G. B., & Horner, D. J. 2004, ApJ, 613, 811  
 Mittal, R., Hudson, D. S., Reiprich, T. H., & Clarke, T. 2009, A&A, 501, 835 (M09)  
 Navarro, J. F., Frenk, C. S., & White, S. D. M. 1995, MNRAS, 275, 720  
 Novicki, M. C., Sornig, M., & Henry, J. P. 2002, AJ, 124, 2413  
 O'Hara, T. B. et al. 2006, ApJ, 639, 64  
 Osmond, J. P. F. & Ponman, T. J. 2004, MNRAS, 350, 1511  
 Poole, G. B., Babul, A., McCarthy, I. G., et al. 2007, MNRAS, 380, 437  
 Pratt, G. W., Croston, J. H., Arnaud, M., & Böhringer, H. 2009, A&A, 498, 361  
 Puchwein, E., Sijacki, D., & Springel, V. 2008, ApJ, 687, L53  
 Reiprich, T. H. 2006, A&A, 453, L39  
 Reiprich, T. H. & Böhringer, H. 2002, ApJ, 567, 716  
 Rosati, P., Borgani, S., & Norman, C. 2002, ARA&A, 40, 539  
 Short, C. J. & Thomas, P. A. 2009, ApJ, 704, 915  
 Sijacki, D. & Springel, V. 2006, MNRAS, 366, 397  
 Stanek, R., Evrard, A. E., Böhringer, H., Schuecker, P., & Nord, B. 2006, ApJ, 648, 956  
 Vikhlinin, A., Burenin, R. A., Ebeling, H., et al. 2009, ApJ, 692, 1033  
 Voit, G. M. & Bryan, G. L. 2001, Nature, 414, 425  
 Zhang, Y., Finoguenov, A., Böhringer, H., et al. 2007, A&A, 467, 437

**Table 3.** Observations: (1) Cluster name, (2) Virial temperature, (3) Bolometric X-ray luminosity (0.01-40) keV, (4) Bolometric X-ray luminosity (0.01-40) keV within  $r_{\text{cool}}$ , the radius at which the gas cooling time is 7.7 Gyr, (5)  $r_{\text{cool}}$  in kpc, (6)  $r_{\text{cool}}$  in arcminute, (7)  $r_{\text{cool}}$  as a fraction of the virial radius,  $R_{500}$ , and (8) hydrogen column densities. The columns with dashes “–” indicate non-cool-core clusters with  $r_{\text{cool}} = 0$ .

Cluster	$kT_{\text{vir}}$ (keV)	$L_X$ ( $10^{44}$ erg s $^{-1}$ )	$L_{X,\text{cool}}$ ( $10^{44}$ erg s $^{-1}$ )	$r_{\text{cool}}$ (kpc)	$r_{\text{cool}}$ (arcminute)	$r_{\text{cool}}/R_{500}$	$N_{\text{H}}$ $10^{22}$ cm $^{-2}$
A0085	$6.00^{0.11}_{-0.11}$	$12.600 \pm 0.076$	$3.518^{0.020}_{-0.020}$	123.61	1.95	0.080	0.02705
A0119	$5.73^{0.34}_{-0.30}$	$3.920 \pm 0.035$	–	–	–	–	0.03280
A0133	$3.96^{0.08}_{-0.10}$	$2.810 \pm 0.023$	$1.105^{0.012}_{-0.009}$	105.56	1.62	0.084	0.01580
NGC0507	$1.44^{0.08}_{-0.10}$	$0.165 \pm 0.002$	$0.055^{0.001}_{-0.001}$	66.75	3.37	0.088	0.05560
A0262	$2.44^{0.03}_{-0.04}$	$0.793 \pm 0.030$	$0.159^{0.001}_{-0.001}$	68.43	3.48	0.069	0.06380
A0400	$2.26^{0.10}_{-0.12}$	$0.545 \pm 0.006$	–	–	–	–	0.10929
A0399	$6.70^{0.14}_{-0.14}$	$9.590 \pm 0.518$	–	–	–	–	0.10700
A0401	$8.51^{0.34}_{-0.22}$	$17.700 \pm 0.194$	–	–	–	–	0.10282
A3112	$4.73^{0.12}_{-0.12}$	$8.710 \pm 0.096$	$4.137^{0.032}_{-0.032}$	127.89	1.51	0.093	0.01270
NGC1399	$1.34^{0.01}_{-0.01}$	$0.053 \pm 0.003$	$0.005^{0.000}_{-0.000}$	19.34	3.43	0.026	0.01523
2A0335	$3.53^{0.10}_{-0.13}$	$4.080 \pm 0.033$	$3.204^{0.025}_{-0.025}$	141.40	3.44	0.119	0.24798
IIIIZw54	$2.50^{0.05}_{-0.06}$	$0.545 \pm 0.042$	$0.065^{0.003}_{-0.003}$	44.79	1.30	0.045	0.14700
A3158	$4.99^{0.07}_{-0.07}$	$6.910 \pm 0.104$	–	–	–	–	0.01210
A0478	$7.34^{0.18}_{-0.19}$	$25.600 \pm 0.154$	$17.23^{0.054}_{-0.070}$	178.08	1.82	0.104	0.29276
NGC1550	$1.34^{0.01}_{-0.01}$	$0.205 \pm 0.011$	$0.097^{0.003}_{-0.003}$	72.15	4.84	0.098	0.13778
EXO0422	$2.93^{0.13}_{-0.12}$	$1.760 \pm 0.109$	$0.713^{0.016}_{-0.016}$	85.24	1.83	0.079	0.08080
A3266	$9.45^{0.35}_{-0.36}$	$12.300 \pm 0.086$	$0.009^{0.001}_{-0.001}$	9.72	0.14	0.005	0.01840
A0496	$4.86^{0.06}_{-0.06}$	$3.780 \pm 0.026$	$1.458^{0.005}_{-0.005}$	102.05	2.62	0.073	0.04279
A3376	$3.80^{0.11}_{-0.10}$	$2.130 \pm 0.030$	–	–	–	–	0.04420
A3391	$5.77^{0.31}_{-0.36}$	$2.870 \pm 0.054$	–	–	–	–	0.05620
A3395s	$4.82^{0.26}_{-0.26}$	$2.460 \pm 0.093$	–	–	–	–	0.07340
A0576	$4.09^{0.09}_{-0.10}$	$1.900 \pm 0.129$	$0.122^{0.003}_{-0.003}$	45.16	0.99	0.035	0.05460
A0754	$11.13^{0.39}_{-0.43}$	$6.620 \pm 0.106$	–	–	–	–	0.05130
A0780	$3.45^{0.08}_{-0.09}$	$6.060 \pm 0.036$	$2.889^{0.007}_{-0.007}$	116.26	1.87	0.099	0.05005
A1060	$3.16^{0.04}_{-0.04}$	$0.581 \pm 0.019$	$0.088^{0.001}_{-0.001}$	43.41	2.84	0.039	0.05030
A1367	$3.58^{0.06}_{-0.06}$	$1.130 \pm 0.009$	–	–	–	–	0.01719
MKW4	$2.01^{0.04}_{-0.04}$	$0.275 \pm 0.005$	$0.076^{0.001}_{-0.001}$	58.50	2.44	0.065	0.01710
ZwCl1215	$6.27^{0.32}_{-0.29}$	$6.250 \pm 0.081$	–	–	–	–	0.01760
NGC4636	$0.90^{0.02}_{-0.02}$	$0.014 \pm 0.001$	$0.006^{0.000}_{-0.000}$	39.40	8.68	0.065	0.01850
A3526	$3.92^{0.02}_{-0.02}$	$1.370 \pm 0.030$	$0.366^{0.004}_{-0.004}$	77.53	5.60	0.062	0.08540
A1644	$5.09^{0.09}_{-0.09}$	$4.090 \pm 0.209$	$0.292^{0.005}_{-0.004}$	69.69	1.27	0.049	0.03990
A1650	$5.81^{0.06}_{-0.07}$	$9.550 \pm 0.630$	$2.333^{0.012}_{-0.012}$	94.52	1.01	0.062	0.01300
A1651	$6.34^{0.27}_{-0.27}$	$9.860 \pm 0.118$	$2.475^{0.050}_{-0.052}$	97.56	1.03	0.061	0.01460
A1656	$9.15^{0.17}_{-0.17}$	$11.100 \pm 0.156$	–	–	–	–	0.00767
NGC5044	$1.22^{0.03}_{-0.04}$	$0.115 \pm 0.001$	$0.089^{0.002}_{-0.002}$	85.46	8.06	0.122	0.05060
A1736	$3.12^{0.11}_{-0.12}$	$2.920 \pm 0.184$	–	–	–	–	0.04315
A3558	$4.95^{0.13}_{-0.15}$	$7.620 \pm 0.038$	$0.670^{0.012}_{-0.012}$	67.96	1.22	0.048	0.03997
A3562	$4.43^{0.21}_{-0.16}$	$3.350 \pm 0.030$	$0.150^{0.006}_{-0.006}$	46.69	0.82	0.035	0.03999
A3571	$7.00^{0.13}_{-0.12}$	$10.200 \pm 0.071$	$2.556^{0.017}_{-0.017}$	65.49	1.43	0.039	0.04382

**Table 3.** continued.

Cluster	$kT_{\text{vir}}$ (keV)	$L_X$ ( $10^{44}$ erg s $^{-1}$ )	$L_{X,\text{cool}}$ ( $10^{44}$ erg s $^{-1}$ )	$r_{\text{cool}}$ (kpc)	$r_{\text{cool}}$ (arcminute)	$r_{\text{cool}}/R_{500}$	$N_{\text{H}}$ $10^{22}$ cm $^{-2}$
A1795	$6.08^{0.07}_{-0.07}$	$14.800 \pm 0.044$	$6.095^{0.016}_{-0.018}$	137.63	1.93	0.088	0.01015
A3581	$1.97^{0.07}_{-0.07}$	$0.544 \pm 0.017$	$0.281^{0.005}_{-0.005}$	87.82	3.19	0.099	0.04310
MKW8	$3.00^{0.12}_{-0.12}$	$0.692 \pm 0.058$	—	—	—	—	0.02340
RXJ1504	$9.53^{1.39}_{-1.16}$	$112.000 \pm 1.120$	$53.875^{0.249}_{-0.249}$	234.84	1.13	0.120	0.06080
A2029	$8.26^{0.09}_{-0.09}$	$27.600 \pm 0.166$	$12.076^{0.026}_{-0.026}$	142.19	1.64	0.078	0.03214
A2052	$3.35^{0.02}_{-0.02}$	$2.180 \pm 0.022$	$1.052^{0.005}_{-0.005}$	104.70	2.50	0.090	0.02680
MKW3S	$3.90^{0.09}_{-0.09}$	$2.690 \pm 0.027$	$1.214^{0.009}_{-0.009}$	92.47	1.76	0.074	0.02860
A2065	$5.40^{0.20}_{-0.11}$	$6.650 \pm 0.406$	$1.061^{0.013}_{-0.012}$	85.95	1.05	0.058	0.03285
A2063	$3.77^{0.06}_{-0.06}$	$2.060 \pm 0.027$	$0.349^{0.004}_{-0.004}$	64.93	1.58	0.053	0.02730
A2142	$8.40^{1.01}_{-0.76}$	$36.100 \pm 0.324$	$7.804^{0.043}_{-0.044}$	125.73	1.25	0.068	0.04151
A2147	$4.07^{0.11}_{-0.12}$	$3.100 \pm 0.099$	—	—	—	—	0.02823
A2163	$15.91^{0.81}_{-0.81}$	$75.500 \pm 1.130$	—	—	—	—	0.11765
A2199	$4.37^{0.07}_{-0.07}$	$4.030 \pm 0.072$	$1.644^{0.008}_{-0.008}$	97.99	2.74	0.074	0.00857
A2204	$8.92^{0.72}_{-0.61}$	$39.600 \pm 0.634$	$23.886^{0.177}_{-0.237}$	171.08	1.09	0.090	0.05921
A2244	$5.78^{0.10}_{-0.11}$	$11.700 \pm 0.246$	$3.758^{0.025}_{-0.022}$	119.86	1.13	0.079	0.01908
A2256	$7.61^{0.65}_{-0.63}$	$11.200 \pm 0.156$	—	—	—	—	0.04566
A2255	$5.81^{0.19}_{-0.20}$	$7.510 \pm 0.090$	—	—	—	—	0.02493
A3667	$6.39^{0.04}_{-0.04}$	$12.600 \pm 0.088$	$0.015^{0.000}_{-0.000}$	12.39	0.19	0.008	0.04590
S1101	$2.57^{0.12}_{-0.13}$	$3.130 \pm 0.028$	$2.368^{0.027}_{-0.026}$	171.11	2.57	0.169	0.01050
A2589	$3.89^{0.05}_{-0.05}$	$1.780 \pm 0.023$	$0.371^{0.003}_{-0.003}$	72.72	1.50	0.058	0.02880
A2597	$4.05^{0.07}_{-0.07}$	$7.320 \pm 0.088$	$4.429^{0.016}_{-0.016}$	125.34	1.32	0.098	0.02200
A2634	$3.19^{0.11}_{-0.11}$	$0.946 \pm 0.015$	$0.004^{0.000}_{-0.000}$	12.03	0.32	0.011	0.05140
A2657	$3.52^{0.12}_{-0.11}$	$1.640 \pm 0.015$	$0.186^{0.006}_{-0.006}$	51.03	1.08	0.043	0.05915
A4038	$3.14^{0.03}_{-0.04}$	$1.900 \pm 0.025$	$0.614^{0.013}_{-0.013}$	82.24	2.31	0.073	0.01540
A4059	$4.22^{0.03}_{-0.03}$	$3.140 \pm 0.041$	$1.169^{0.005}_{-0.005}$	109.85	1.99	0.084	0.01058